Anisotropic Laplace-Beltrami Eigenmaps: Bridging Reeb Graphs and Skeletons

Yonggang Shi[1], Rongjie Lai[2], Sheila Krishna[3], Nancy Sicotte[3], Ivo Dinov[1], Arthur W. Toga[1*]
[1]Lab of Neuro Imaging, UCLA School of Medicine, Los Angeles, CA, USA
[2]Department of Mathematics, UCLA, Los Angeles, CA, USA
[3]Department of Neurology, UCLA School of Medicine, Los Angeles, CA, USA
yshi@loni.ucla.edu

Abstract

In this paper we propose a novel approach of computing skeletons of robust topology for simply connected surfaces with boundary by constructing Reeb graphs from the eigenfunctions of an anisotropic Laplace-Beltrami operator. Our work brings together the idea of Reeb graphs and skeletons by incorporating a flux-based weight function into the Laplace-Beltrami operator. Based on the intrinsic geometry of the surface, the resulting Reeb graph is pose independent and captures the global profile of surface geometry. Our algorithm is very efficient and it only takes several seconds to compute on neuroanatomical structures such as the cingulate gyrus and corpus callosum. In our experiments, we show that the Reeb graphs serve well as an approximate skeleton with consistent topology while following the main body of conventional skeletons quite accurately.

1. Introduction

Skeletons are important tools in studying shapes[2] as they provide an intuitive graph representation that connects well with high level understandings. The challenge of using skeletons in group studies is to maintain a consistent topology across population. In this paper, we propose a novel approach of computing skeletons with consistent topology on simply connected surface patches in 3D by constructing a Reeb graph from the eigenfunction of an anisotropic Laplace-Beltrami operator.

One weakness in using skeletons to represent shapes is their sensitivity to small changes on the boundary, which makes it difficult to compare a group of shapes belonging to the same category but having subtle differences. As an example, we show the skeletons of four cingulate gyri in Fig. 1 that are computed with the method of Hamilton-Jacobi skeletons[18]. While the skeletons are relatively clean, they have different graph structures. To address this challenge, various approaches were proposed to enforce a consistent topology on the skeleton. A skeleton of fixed topology was computed for 2D shapes by driving a snake model to the shocks in the distance map[5]. A similar approach was also taken in studying 3D shapes with a medial axis [20]. Pruning strategies based on continuity and significance were also developed to simplify skeletons [10, 19, 3]. The other powerful approach is the M-rep that uses a generative approach to match templates designed a priori to new shapes [11]. More recently, the idea of inverse skeletonization was used to compute skeletons of simplified topology via the solution of a nonlinear optimization problem [22].

Given a function defined on a surface, its Reeb graph is intuitively a graph describing the neighboring relation of the level sets of the function. Following Morse theory, Reeb graphs [13] have been used as a powerful tool to analyze geometric information contained in various sources of imaging data. A Reeb graph was constructed to build a smooth surface interpolating a series of contour lines [17]. Contour trees were constructed to store seed information for efficient visualization of volume images [21]. The Reeb graphs were also used to study terrain imaging data [1] and the matching of topological information in a database of 3D shapes [6].

In this paper, we propose to use Reeb graphs to construct a skeleton of robust topology for simply connected surface patches with the aim of studying anatomical structures such as the cingulate gyrus and corpus callosum. There are two main contributions in our work. First of all, we propose to use the spectrum of the Laplace-Beltrami operator[14, 12] to construct the Reeb graph, which ensures the Reeb graph is invariant to the pose of the shape. Our second contribution is the development of an anisotropic Laplace-Beltrami operator based on a flux measure[18]. This bridges the idea of Reeb graphs with conventional skeletons and makes the Reeb graphs follow the main body of skeletons.

The rest of the paper is organized as follows. In sec-

*This work was funded by the National Institutes of Health through the NIH Roadmap for Medical Research, Grant U54 RR021813 entitled Center for Computational Biology (CCB). Information on the National Centers for Biomedical Computing can be obtained from http://nihroadmap.nih.gov/bioinformatics.

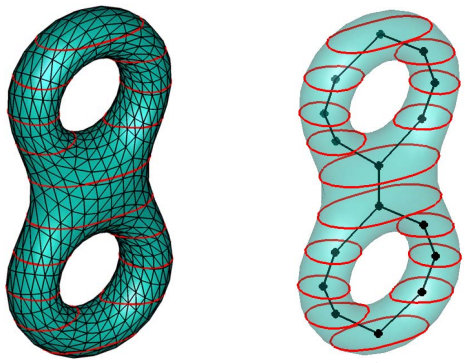

(a) (b)

Figure 2. The Reeb graph of the height function on a double torus of genus two. (a) Level sets of the height function. (b) The Reeb graph of the level sets.

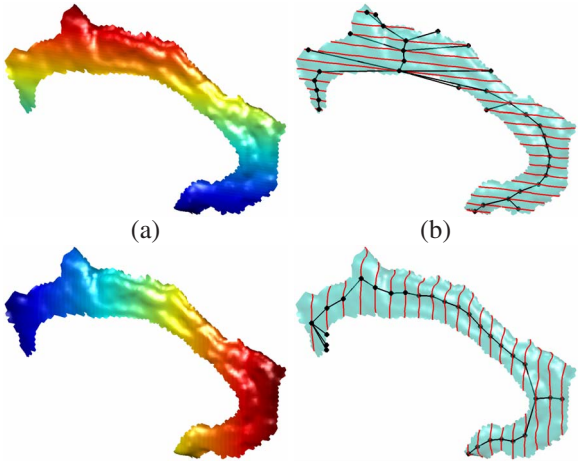

(a) (b) (c) (d)

Figure 3. The Reeb graphs of two different feature functions f on a cingulate gyrus. (a) f is the z-coordinates; (b) The Reeb graph from the function f in (a); (c) f is the y-coordinates; (d) The Reeb graph from the function f in (c).

tion 2, we introduce the mathematical background of Reeb graphs and its construction on triangular meshes. We describe the spectrum of the anisotropic Laplace-Beltrami operator and its use of building Reeb graphs in section 3. After that, a flux-based weight function is proposed in section 4 to define the anisotropic Laplace-Beltrami operator. Experimental results are presented in section 5. Finally conclusions are made in section 6.

2. Reeb Graphs

Let $\mathcal{M}$ denote a compact surface and a feature function f defined on this surface. The Reeb graph of f on $\mathcal{M}$ is defined as follows.

Definition 1 *Let $f : \mathcal{M} \to \mathbb{R}$. The Reeb graph $R(f)$ of f is the quotient space with its topology defined through the equivalent relation $x \simeq y$ if $f(x) = f(y)$ for $\forall x, y \in \mathcal{M}$.*

As a quotient topological space derived from $\mathcal{M}$, the connectivity of the elements in $R(f)$, which are the level sets of f, is determined by the topology, i.e., the collection of open sets, of $\mathcal{M}$. If f is a Morse function [7], which means the critical points of f are non-degenerative, the Reeb graph $R(f)$ encodes the topology of $\mathcal{M}$ and it has g loops for a manifold of genus g.

To compute the Reeb graph numerically, we assume the surface $\mathcal{M}$ is represented as a triangular mesh $\mathcal{M} = (\mathcal{V}, \mathcal{T})$, where $\mathcal{V}$ and $\mathcal{T}$ are the set of vertices and triangles, respectively. The function f is then defined on each vertex in $\mathcal{V}$. We sample the level sets of f at a set of K values $\xi_0 < \xi_1 < \cdots < \xi_{K-1}$ and the set of contours as

$$\Gamma = \{\Gamma_k^l, 0 \le k \le K-1, 0 \le l \le L_k, \}$$

where L_k denotes the number of contours at the level ξ_k, and Γ_k^l represents the l-th contour at this level. To build edges between contours at neighboring levels, we consider the region

$$R_{k,k+1} = \{x \in \mathcal{M} | \xi_k \le f(x) \le \xi_{k+1}\}$$

and a contour $\Gamma_k^{l_1}$ at the level ξ_k and a contour $\Gamma_{k+1}^{l_2}$ at the level ξ_{k+1} are connected if they belong to the same connected component in $R_{k,k+1}$. This completes the construction of a Reeb graph on $\mathcal{M}$ as an undirected graph with the level contours as the nodes and the edges representing the neighboring relation of these contours.

As an example, we illustrate the construction of a Reeb graph on a double torus shown in Fig. 2(a). The feature function f used here is the height function. We sample ten level sets of f and plot them as red contours on the surface. With these contours as its nodes, the Reeb graph is shown in Fig. 2(b), where the centroid of each contour is used to explicitly represent the nodes of the graph. Clearly this graph has two loops and it captures the topology of the shape.

Reeb graphs can also be constructed for functions defined on surfaces with boundary. For the cingulate gyrus on a left hemispherical surface, we compute the Reeb graph for two different choices of the feature function f. In Fig. 3(a) and (c), the function f is the z- and y- coordinates of vertices, respectively. For these two functions, we sample 20 level sets and the resulting Reeb graphs are shown in Fig. 3(b) and (d), respectively. Since the level sets here are curve segments, we use the middle point of each curve segment to explicitly represent the node of the Reeb graph.

The above results demonstrate that Reeb graphs can be constructed successfully on surface patches given a feature function f, but they also help point out the main difficulty in using Reeb graphs to compare shapes across population: the selection of an appropriate feature function f. The two feature functions used above are similar to the height function used commonly in previous work [1] and there are two

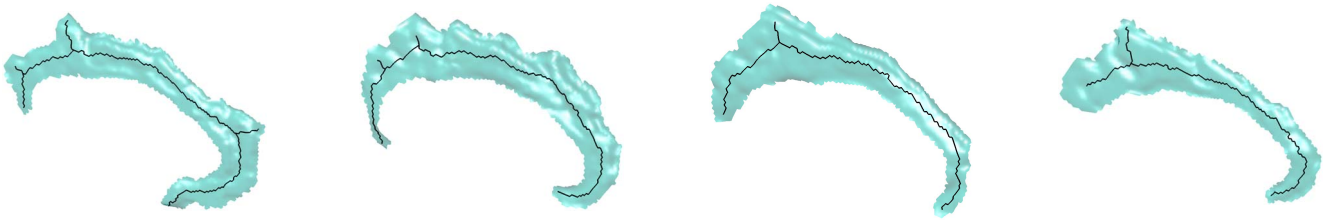

(a) (b) (c) (d)

Figure 1. The Hamilton-Jacobi skeleton of four cingulate gyri.

drawbacks of such choices. First, their Reeb graphs are pose dependent as the coordinates will change under rotation. Second, they are sensitive to noise on the boundary. We can see in Fig. 3(b) and (d) that spurious branches are created in the Reeb graphs because the boundary is jaggy as is pretty common for manually segmented structures. We next propose to use the eigenfunctions of an anisotropic Laplace-Beltrami operator as the feature function, which are defined intrinsically on the surface and robust to irregularities on the boundary.

3. Anisotropic Laplace-Beltrami Eigenmaps

In this section, we introduce the anisotropic Laplace-Beltrami operator on a surface patch and the computation of its spectrum. We then propose to use the first nontrivial eigenfunction of this operator as the feature function in the construction of Reeb graphs.

The spectrum of the Laplace-Beltrami operator has been used in several work in medical imaging [12, 9]. Here we consider the more general anisotropic Laplace-Beltrami operator $\nabla_{\mathcal{M}} \cdot (w \nabla_{\mathcal{M}})$ on a simply connected surface patch $\mathcal{M}$, where $\nabla_{\mathcal{M}}$ is the intrinsic gradient operator on $\mathcal{M}$, and $w : \mathcal{M} \rightarrow \mathbb{R}^+$ is the weight defined over $\mathcal{M}$. If we set $w = 1$, we have the regular Laplace-Beltrami operator. Here we only require w to be positive to ensure the operator is elliptic, so the spectrum is discrete and can be expressed as follows. We denote the set of eigenvalues as $0 \leq \lambda_0 \leq \lambda_1 \leq \cdots$ and the corresponding eigenfunctions as $f_0, f_1, \cdots$ such that

$$\nabla_{\mathcal{M}} \cdot (w \nabla_{\mathcal{M}} f_n) = \lambda_n f_n, \;\; n = 0, 1, \cdots \tag{1}$$

The set of eigenfunctions form orthonormal basis functions on $\mathcal{M}$ and can be intuitively considered as the intrinsic Fourier basis functions on the surface. In fact, they have been used for denoising in brain imaging studies [12].

To compute the spectrum, we use the weak form of (1). Taking the Neumann boundary condition, we can find the eigenvalues as the critical points of the following energy

$$E(f) = \frac{\int_{\mathcal{M}} w \parallel \nabla_{\mathcal{M}} f \parallel^2 d\mathcal{M}}{\int_{\mathcal{M}} \parallel f \parallel^2 d\mathcal{M}}. \tag{2}$$

For numerical implementation, we assume $\mathcal{M} = (\mathcal{V}, \mathcal{T})$ is a triangular mesh, where $\mathcal{V} = \{\mathcal{V}_i | i = 1, \cdots, N_v\}$ and $\mathcal{T} = \{\mathcal{T}_i | i = 1, \cdots, N_t\}$ are the set of vertices and triangles. The weight w and the eigenfunction f are assumed to be piece-wise linear and defined on vertices, so we can represent them as vectors of size $N_v \times 1$. Using the method of finite elements on triangular meshes, we can convert the integral in (2) into the matrix form

$$E = \frac{f' Q_w f}{f' K f} \tag{3}$$

where both Q_w and K are matrices of size $N_v \times N_v$. The matrix Q_w takes into account the integral $\int_{\mathcal{M}} w \parallel \nabla_{\mathcal{M}} f \parallel^2 d\mathcal{M}$ and its element $Q_w(i,j)(1 \leq i, j \leq N_v)$ is defined as:

$$Q_w(i,j) = \begin{cases} \frac{1}{2} \sum\limits_{\mathcal{V}_j \in N(\mathcal{V}_i)} \sum\limits_{\mathcal{T}_k \in N(\mathcal{V}_i, \mathcal{V}_j)} w_k \cot \theta_k^{i,j}, & \text{if } i = j; \\ -\frac{1}{2} \sum\limits_{\mathcal{T}_k \in N(\mathcal{V}_i, \mathcal{V}_j)} w_k \cot \theta_k^{i,j}, & \text{if } \mathcal{V}_j \in N(\mathcal{V}_i); \\ 0, & \text{otherwise.} \end{cases}$$

Here $N(\mathcal{V}_i)$ is the set of vertices in the 1-ring neighborhood of $\mathcal{V}_i$, $N(\mathcal{V}_i, \mathcal{V}_j)$ is the set of triangles sharing the edge $(\mathcal{V}_i, \mathcal{V}_j)$, $\theta_k^{i,j}$ is the angle in the triangle $\mathcal{T}_k$ opposite to the edge $(\mathcal{V}_i, \mathcal{V}_j)$, and the weight w_k on each triangle $\mathcal{T}_k$ is defined as

$$w_k = \frac{1}{3} \sum_{\mathcal{V}_i \in \mathcal{T}_k} w(\mathcal{V}_i). \tag{4}$$

The matrix K represents the integral $\int_{\mathcal{M}} \parallel f \parallel^2 d\mathcal{M}$ and its element $K(i,j)(1 \leq i, j \leq N_v)$ is defined as:

$$K(i,j) = \begin{cases} \frac{1}{12} \sum\limits_{\mathcal{V}_j \in N(\mathcal{V}_i)} \sum\limits_{\mathcal{T}_k \in N(\mathcal{V}_i, \mathcal{V}_j)} A_k, & \text{if } i = j; \\ \frac{1}{12} \sum\limits_{\mathcal{T}_k \in N(\mathcal{V}_i, \mathcal{V}_j)} A_k, & \text{if } \mathcal{V}_j \in N(\mathcal{V}_i); \\ 0, & \text{otherwise,} \end{cases}$$

where A_k is the area of the k-th triangle $\mathcal{T}_k$.

Using the matrix representation in (3), we compute the spectrum of $\nabla_{\mathcal{M}} \cdot (w \nabla_{\mathcal{M}})$ via solving a generalized matrix

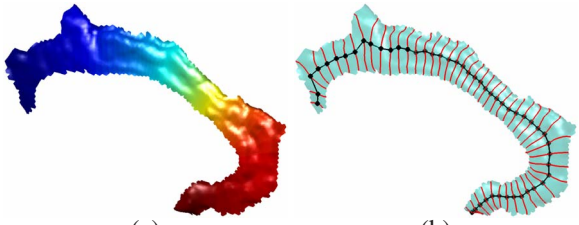

(a) (b)

Figure 4. The Reeb graph of the Laplace-Beltrami eigenmap. (a) The eigenmap. (b) The level sets of the eigenmap and the Reeb graph.

eigenvalue problem:

$$Q_w f = \lambda K f. \tag{5}$$

This problem can be solved with a variety of numerical linear algebra packages. In our implementation, we represent both Q_w and K as sparse matrices and use Matlab to solve (5). Since the sum of each row in Q_w equals zero, the first eigenvalue $\lambda_0 = 0$ and f_0 is constant. As the first nontrivial eigenfunction, f_1 minimizes the energy E and achieves the critical value at λ_1:

$$\lambda_1 = \int_{\mathcal{M}} w \parallel \nabla_{\mathcal{M}} f_1 \parallel^2 d\mathcal{M}, \tag{6}$$
$$s.t. \quad \parallel f_1 \parallel^2 = 1.$$

Thus the eigenmap f_1 provides the smoothest, non-constant map from $\mathcal{M}$ to $\mathbb{R}$. Using this eigenmap, we can capture the intrinsic structure of elongated shapes such as the cingulate gyrus and corpus callosum. The eigenmap is also invariant under isometric transformations such as bending.

As an example, the eigenmap f_1 with the isotropic weight $w = 1$ for the cingulate gyrus in Fig. 3 is visualized in Fig. 4(a). The level sets of this function are plotted as red contours in Fig. 4(b), where the Reeb graph is computed with each node representing the middle point of the level sets. From the level sets, we can see the eigenmap f_1 projects the surface smoothly onto $\mathbb{R}$ and is robust to the jaggy boundary of the surface. Compared with the skeleton in Fig. 1(a), we can see the Reeb graph of f_1 has a simple chain structure and approximates the main component of the skeleton very well.

4. Flux-based Weight Functions

In the cingulate gyrus example in section 3, we see that the Laplace-Beltrami eigenmap provides a robust way of constructing the Reeb graph and capturing the global structure of the shape. In some cases, however, the Reeb graph built from the eigenmap of the isotropic Laplace-Beltrami operator is insufficient as an approximation of the skeleton. We show such an example in Fig. 5. The Hamilton-Jacobi skeleton of the corpus callosum is plotted in Fig. 5(a), and the Reeb graph of the eigenmap f_1 computed with the isotropic weight $w = 1$, together with the level sets, is shown in Fig. 5(b). For most parts, the Reeb graph does a good job in approximating the skeleton, but it is also not hard to notice that it fails to follow the bending of the genu at the frontal end of the corpus callosum, which is well represented in the conventional skeleton in Fig. 5(a). In this section, we design a weight function to incorporate information in skeletons into the construction of Reeb graphs.

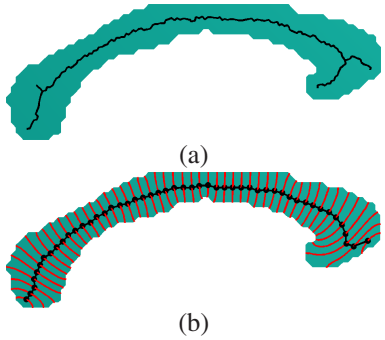

(a)

(b)

Figure 5. The Reeb graph of a corpus callosum using the eigenmap of the isotropic Laplace-Beltrami operator. (a) The Hamilton-Jacobi skeleton. (b) The Reeb graph.

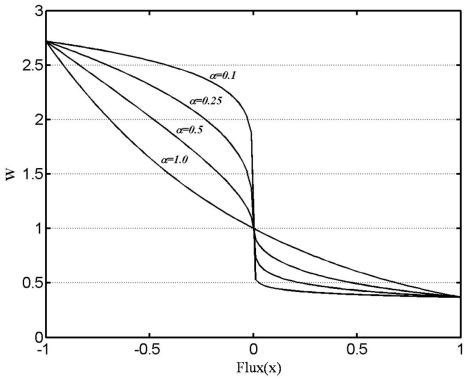

Figure 6. The weight function.

The weight function we choose is based on the flux measure used in the method of Hamilton-Jacobi skeleton [18] and its extension to triangular meshes [16]. For a surface patch $\mathcal{M}$, let $\partial\mathcal{M}$ denote its boundary. We define a distance transform $D : \mathcal{M} \rightarrow \mathbb{R}$ as:

$$D(x) = \min_{y \in \partial\mathcal{M}} d(x, y) \;\; \forall x \in \mathcal{M} \tag{7}$$

where $d(\cdot, \cdot)$ is the geodesic distance between two points. Given this distance transform, the flux measure is defined as

$$Flux(x) = \frac{\int_{\delta R} < \vec{N}, \nabla_{\mathcal{M}} D > ds}{\int_{\delta R} ds} \;\; \forall x \in \mathcal{M} \tag{8}$$

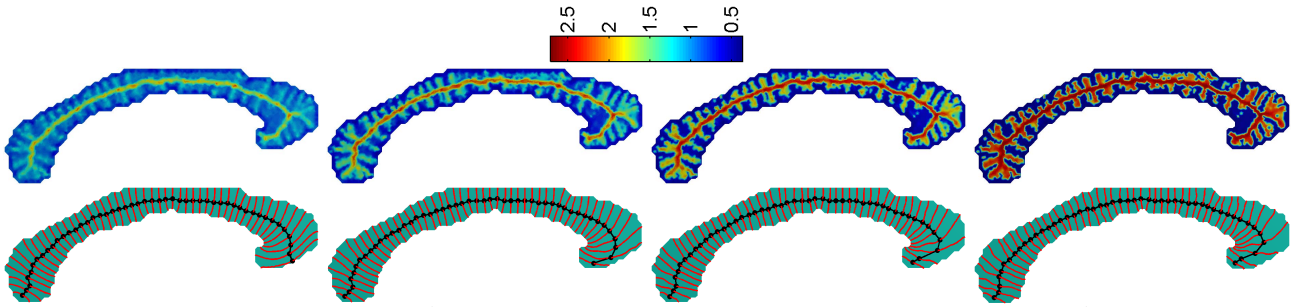

(a) $\alpha = 1.0$. (b) $\alpha = 0.5$. (c) $\alpha = 0.25$. (d) $\alpha = 0.1$.

Figure 7. The effects of the parameter α on the Reeb graph. Top row: the weight function mapped onto the surface. Bottom row: the level sets and the Reeb graph of the anisotropic Laplace-Beltrami eigenmap.

where δR is the boundary of an infinitesimal geodesic neighborhood of x, $\vec{N}$ is the outward normal direction of δR and $\nabla_{\mathcal{M}} D$ is the intrinsic gradient of D on $\mathcal{M}$.

To numerically compute the flux measure for a triangular mesh, we first compute the distance transform with the fast marching algorithm on triangular meshes [8] to solve the Eikonal equation on $\mathcal{M}$:

$$\|\nabla_{\mathcal{M}} D\| = 1. \tag{9}$$

We then calculate the flux measure at each vertex of $\mathcal{M}$ as:

$$Flux(\mathcal{V}_i) \approx \frac{1}{\sharp N(\mathcal{V}_i)} \sum_{\mathcal{V}_j \in N(\mathcal{V}_i)} < \frac{\overrightarrow{\mathcal{V}_i \mathcal{V}_j}}{\| \overrightarrow{\mathcal{V}_i \mathcal{V}_j} \|}, \nabla_{\mathcal{M}} D(\mathcal{V}_j) > \tag{10}$$

where $\sharp N(\mathcal{V}_i)$ is the number of vertices in the 1-ring neighborhood $N(\mathcal{V}_i)$ of $\mathcal{V}_i$, and $\overrightarrow{\mathcal{V}_i \mathcal{V}_j}$ is the vector from the vertex $\mathcal{V}_i$ to $\mathcal{V}_j$.

Based on the flux measure, we define the weight function as:

$$w(x) = e^{-sign(Flux(x))|Flux(x)|^{\alpha}} \quad \forall x \in \mathcal{M}. \tag{11}$$

Following this definition, more weight is given to points on the skeleton as the flux is more negative at these points according to (10). Recall that the eigenmap f_1 is the smoothest projection from $\mathcal{M}$ to $\mathbb{R}$ by the minimization of the energy in (7). As we decrease the parameter α, as shown in Fig. 6, we put more weight on vertices close to the skeleton, and the shape looks more like the skeleton for the energy in (7). Thus intuitively the projection from $\mathcal{M}$ to $\mathbb{R}$ will happen along the skeleton and the level sets of the eigenmap should be more oriented in the direction normal to the skeleton.

With each of the four weight functions in Fig. 6, we compute the eigenmap of the anisotropic Laplace-Beltrami operator $\nabla_{\mathcal{M}} \cdot (w \nabla_{\mathcal{M}})$ and use it to construct a Reeb graph for the corpus callosum in Fig. 5. The weight functions and the corresponding Reeb graphs are shown in Fig. 7. As we decrease the parameter α from 1.0 to 0.1, we can see the level sets of the eigenmap at the frontal part turn more toward the direction pointed by the main body of the skeleton. As a result, the Reeb graph follows the bending of the genu better than simply using the isotropic Laplace-Beltrami operator.

5. Experimental Results

In this section, we present experimental results to demonstrate our algorithm. Reeb graphs are constructed on two anatomical structures: the cingulate gyrus and corpus callosum. We illustrate that our algorithm can be used as an efficient and robust approach of computing skeletons of consistent topology for these shapes.

In the first experiment, we apply our algorithm to a group of 16 cingulate gyri as shown in Fig. 8 with the weight function $w = 1$. Each surface patch is extracted from triangulated cortical surfaces with manual labeling, and it is usually composed of around 2000 vertices and 4000 triangles. The computational time is less than 2 seconds on a PC. For each shape, we sample the eigenmap at 50 level sets and use the middle point of each level contour as the node of the Reeb graph. Intuitively we can see the Reeb graphs successfully capture the global profile of these elongated surface patches. For all the examples, the Reeb graphs have the same chain structure.

In the second experiment, we compute Reeb graphs for a group of 16 corpora callosa with an anisotropic Laplace-Beltrami eigenmap by choosing the parameter $\alpha = 0.25$ in (11). The surface patch of each corpus callosum is constructed from manually labeled binary masks with the software triangle [15] and also composed of around 2000 vertices and 4000 triangles. Because of the need of calculating the weight function, it takes around 3 seconds, which is slightly longer than using the isotropic Laplace-Beltrami eigenmaps, to compute the Reeb graphs on a PC. Similar to the cingulate examples, a collection of 50 level sets are sampled on the eigenmap of each corpus callosum. From the results shown in Fig. 9, we can see all the Reeb graphs

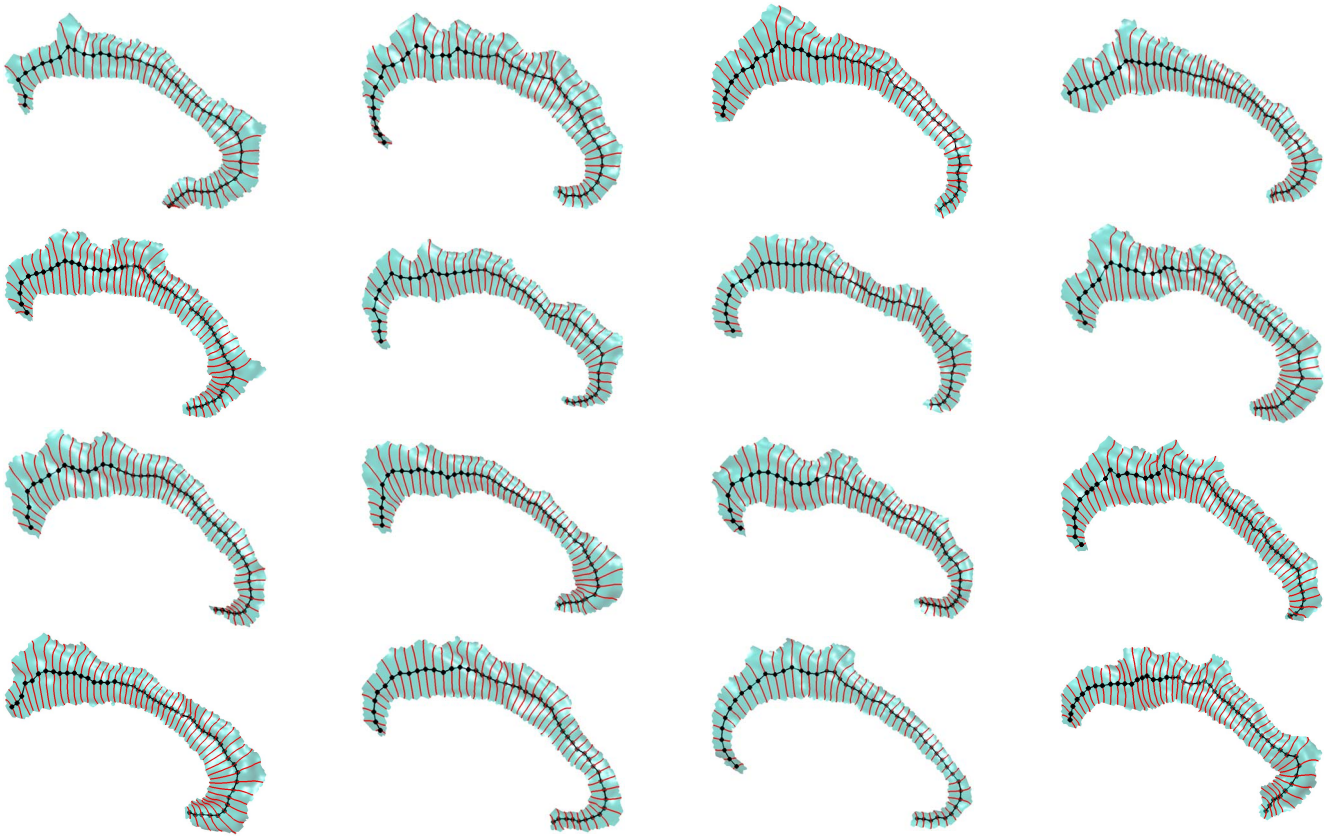

Figure 8. The Reeb graph of 16 cingulate gyri constructed using the Laplace-Beltrami eigenmap.

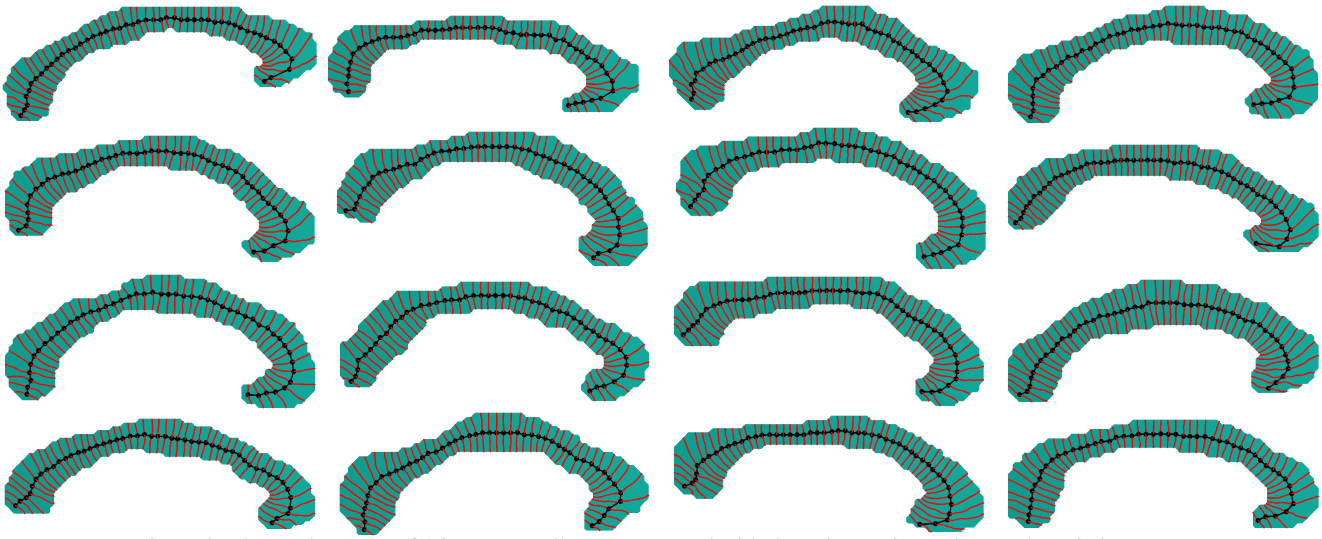

Figure 9. The Reeb graphs of 16 corpora callosa constructed with the anisotropic Laplace-Beltrami eigenmap.

have the chain structure and successfully capture the bending of the genu.

To measure the advantage of using the anisotropic eigenmap for analyzing the corpus callosum, we have also computed the Reeb graphs with the isotropic weight $w = 1$ for the 16 corpora callosa. After factoring out rotation and translation, we applied a principal component analysis (PCA) to each of the two groups of Reeb graphs [4]. The variances of the principal components for both the isotropic and anisotropic Reeb graphs are plotted in Fig. 10. We can see clearly the anisotropic Reeb graphs generate more compact representations. This gives a quantitative validation

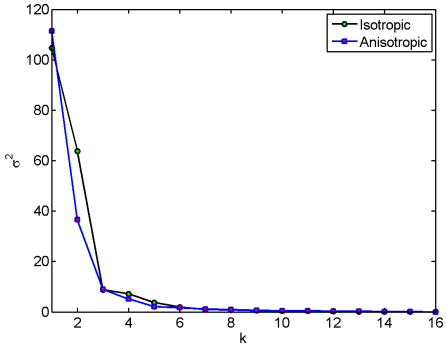

Figure 10. A comparison of the eigenvalue distribution obtained by applying a PCA to Reeb graphs of corpora callosa constructed with both isotropic and anisotropic Laplace-Beltrami eigenmaps.

that anatomically meaningful features are better aligned with the use of the anisotropic Laplace-Beltrami eigenmaps.

6. Conclusions

In this paper, we propose to use the Reeb graph of an anisotropic Laplace-Beltrami eigenmap to analyze shapes represented as simply connected surface patches. Experimental results on two neuroanatomical structures have been presented to demonstrate the use of Reeb graphs as skeletons of consistent topology. Besides shape analysis, the results from our algorithm can also be used to test local morphometry changes with our results by using the length of the level sets as a width measure and the correspondences established by the Reeb graphs. For future work, we will also use the level sets to construct an intrinsic parameterization for the statistical analysis of anatomical/functional features distributed over the structure.

References

[1] S. Biasotti, B. Falcidieno, and M. Spagnuolo. Extended reeb graphs for surface understanding and description. In *Proc. DGCI'00:*, pages 185–197, 2000.

[2] H. Blum and R. Nagel. Shape description using weighted symmetric axis features. *Pattern Recognition*, 10(3):167–180, 1978.

[3] S. Bouix, J. C. Pruessner, D. L. Collins, and K. Siddiqi. Hippocampal shape analysis using medial surfaces. *NeuroImage*, 25(4):1077–1089, 2005.

[4] T. Cootes, C. Taylor, D. Cooper, and J. Graham. Active shape models-their training and application. *Computer Vision and Image Understanding*, 61(1):38–59, 1995.

[5] P. Golland, W. Grimson, and R. Kikinis. Statistical shape analysis using fixed topology skeletons: Corpus callosum study. In *Proc. IPMI*, pages 382–387, 1999.

[6] M. Hilaga, Y. Shinagawa, T. Kohmura, and T. L. Kunii. Topology matching for fully automatic similarity estimation of 3d shapes. In *Proc. SIGGRAPH '01*, pages 203–212, 2001.

[7] J. Jost. *Riemannian Geometry and Geometric Analysis*. Springer, 3rd edition, 2001.

[8] R. Kimmel and J. A. Sethian. Computing geodesic paths on manifolds. *Proc. Natl. Acad. Sci. USA*, 95(15):8431–8435, 1998.

[9] M. Niethammer, M. Reuter, F.-E. Wolter, S. Bouix, N. P. M.-S. Koo, and M. Shenton. Global medical shape analysis using the Laplace-Beltrami spectrum. In *Proc. MICCAI*, volume 1, pages 850–857, 2007.

[10] R. L. Ogniewicz and O. Kbler. Hierarchic voronoi skeletons. *Pattern Recognition*, 28(3):343–359, 1995.

[11] S. M. Pizer, D. S. Fritsch, P. A. Yushkevich, V. E. Johnson, and E. L. Chaney. Segmentation, registration, and measurement of shape variation via image object shape. *IEEE Trans. Med. Imag.*, 18(10):851–865, 1999.

[12] A. Qiu, D. Bitouk, and M. I. Miller. Smooth functional and structural maps on the neocortex via orthonormal bases of the laplace-Beltrami operator. *IEEE Trans. Med. Imag.*, 25(10):1296–1306, 2006.

[13] G. Reeb. Sur les points singuliers d'une forme de Pfaff completement integrable ou d'une fonction nemérique. *Comptes Rendus Acad. Sciences*, 222:847–849, 1946.

[14] M. Reuter, F. Wolter, and N. Peinecke. Laplace-Beltrami spectra as Shape-DNA of surfaces and solids. *Computer-Aided Design*, 38:342–366, 2006.

[15] J. R. Shewchuk. Delaunay refinement algorithms for triangular mesh generation. *Comput. Geom. Theory & Applications*, 22(1–3):21–74, 2002.

[16] Y. Shi, P. Thompson, I. Dinov, and A. Toga. Hamilton-Jacobi skeleton on cortical surfaces. *IEEE Trans. Med. Imag.*, 27(5):664–673, 2008.

[17] Y. Shinagawa and T. L. Kunii. Constructing a Reeb graph automatically from cross sections. *IEEE Computer Graphics & Applications*, 11(6):44–51, 1991.

[18] K. Siddiqi, S. Bouix, A. Tannebaum, and S. Zuker. Hamilton-Jacobi skeletons. *Int'l Journal of Computer Vision*, 48(3):215–231, 2002.

[19] M. Styner, G. Gerig, J. Lieberman, D. Jones, and D. Weinberger. Statistical shape analysis of neuroanatomical structures based on medial models. *Med. Image. Anal.*, 7(3):207–220, 2003.

[20] P. M. Thompson, K. M. Hayashi, G. I. de Zubicaray, A. L. Janke, S. E. Rose, J. Semple, M. S. Hong, D. H. Herman, D. Gravano, D. M. Doddrell, and A. W. Toga. Mapping hippocampal and ventricular change in Alzheimer disease. *NeuroImage*, 22(4):1754–1766, 2004.

[21] M. van Kreveld, R. van Oostrum, C. Bajaj, V. Pascucci, and D. Schikore. Contour trees and small seed sets for isosurface traversal. In *Proc. 13th Annu. ACM Sympos. Comput. Geom.*, pages 212–220, 1997.

[22] P. A. Yushkevich, H. Zhang, and J. C. Gee. Continuous medial representation for anatomical structures. *IEEE Trans. Med. Imag.*, 25(12):1547–1564, 2006.